Southern Ocean Overturning Compensation in an Eddy-Resolving Climate Simulation

STUART P. BISHOP

North Carolina State University, Raleigh, North Carolina

PETER R. GENT AND FRANK O. BRYAN

National Center for Atmospheric Research, Boulder, Colorado*

ANDREW F. THOMPSON

California Institute of Technology, Pasadena, California

MATTHEW C. LONG

National Center for Atmospheric Research, Boulder, Colorado*

RYAN ABERNATHEY

Columbia University, New York, New York

(Manuscript received 21 September 2015, in final form 20 January 2016)

ABSTRACT

The Southern Ocean's Antarctic Circumpolar Current (ACC) and meridional overturning circulation (MOC) response to increasing zonal wind stress is, for the first time, analyzed in a high-resolution (0.1° ocean and 0.25° atmosphere), fully coupled global climate simulation using the Community Earth System Model. Results from a 20-yr wind perturbation experiment, where the Southern Hemisphere zonal wind stress is increased by 50% south of 30°S, show only marginal changes in the mean ACC transport through Drake Passage—an increase of 6% [136–144 Sverdrups (Sv; $1\,\mathrm{Sv} \equiv 10^6\,\mathrm{m^3\,s^{-1}}$)] in the perturbation experiment compared with the control. However, the upper and lower circulation cells of the MOC do change. The lower cell is more affected than the upper cell with a maximum increase of 64% versus 39%, respectively. Changes in the MOC are directly linked to changes in water mass transformation from shifting surface isopycnals and sea ice melt, giving rise to changes in surface buoyancy forcing. The increase in transport of the lower cell leads to upwelling of warm and salty Circumpolar Deep Water and subsequent melting of sea ice surrounding Antarctica. The MOC is commonly supposed to be the sum of two opposing components: a wind- and transient-eddy overturning cell. Here, the transient-eddy overturning is virtually unchanged and consistent with a large-scale cancellation of localized regions of both enhancement and suppression of eddy kinetic energy along the mean path of the ACC. However, decomposing the time-mean overturning into a time- and zonal-mean component and a standing-eddy component reveals partial compensation between wind-driven and standing-eddy components of the circulation.

1. Introduction

It is currently estimated that more than 40% of the oceanic uptake of anthropogenic CO_2 takes place south of 40°S (Sallée et al. 2012), and mesoscale eddies play an important role in the uptake (Gnanadesikan et al. 2015). The oceanic uptake over the Southern Ocean is largely governed by the strength of the meridional overturning

* The National Center for Atmospheric Research is sponsored by the National Science Foundation.

Corresponding author address: Stuart P. Bishop, Department of Marine, Earth, and Atmospheric Sciences, North Carolina State University, Campus Box 8208, Raleigh, NC 27695.
E-mail: spbishop@ncsu.edu

DOI: 10.1175/JPO-D-15-0177.1

circulation (MOC) and the location of outcropping isopycnals at the surface (Marshall and Speer 2012; Morrison et al. 2015). Over the past 50 years, Southern Ocean winds have been increasing at a steady rate and have shifted poleward in response to anthropogenic forcing from the Antarctic ozone hole in the lower stratosphere and global climate change (Thompson et al. 2011). Recent work from paleo records suggests that the Southern Ocean winds have been weaker in past climates because of an equatorward shift of the polar Westerlies (Toggweiler 2009) and are currently the strongest they have been in the past 1000 years (Abram et al. 2014). Understanding how the strength of the Antarctic Circumpolar Current (ACC) and MOC respond to changing winds is fundamental to understanding global climate change.

The ACC and MOC response to changing surface wind and buoyancy forcing hinges on the response by mesoscale eddies. One hypothesis is that there will be zero change in ACC transport with increasing winds. The paradigm is that as winds increase, the ACC transport remains roughly constant, because wind-forced steepening of isopycnals will quickly be brought back to their original state. This is accomplished by downgradient eddy buoyancy fluxes, generated via baroclinic instability, that draw on the excess available potential energy imparted by the increase in zonal wind stress. Interfacial form stress, which is proportional to the eddy buoyancy fluxes, then transfers this excess wind-driven momentum to the sea floor where it is balanced by bottom form drag (Ward and Hogg 2011). The near independence of the ACC transport (usually through Drake Passage) to changes in the Southern Hemisphere wind stress is commonly referred to as ''eddy saturation'' (Straub 1993; Munday et al. 2013). Eddy saturation is becoming more widely accepted as limited observations (Firing et al. 2011; Chidichimo et al. 2014; Böning et al. 2008) and modeling efforts (Farneti et al. 2015) see only small trends in ACC transport over multiple decades of increased wind forcing.

It is less clear how the Southern Ocean's zonally integrated meridional circulation responds to changing winds. Theories suggest that the Southern Ocean MOC is the small residual of a near cancelation of two opposing meridional circulation cells; a clockwise (looking west) wind-driven circulation in the density-latitude plane (equatorward at the surface and poleward at depth) known as the ''Deacon cell'' and an eddy-driven cell of opposite sense (Johnson and Bryden 1989; Marshall and Radko 2003). The near independence of the MOC to changes in wind stress is referred to as ''eddy compensation'' because any changes to the wind-driven Deacon cell will be compensated by the eddy-driven circulation. Crucially, any changes in the MOC must be consistent with surface buoyancy modifications, and thus water mass transformation, related to changes in the wind field.

The degree of eddy compensation presently taking place in the Southern Ocean is unknown, but there is observational evidence from satellite altimetry that surface eddy kinetic energy (EKE) has increased in recent decades (Meredith and Hogg 2006; Hogg et al. 2015). Oceanic observations are too sparse to make a direct diagnosis of the MOC so that there is no ''true'' estimate for models to use as a benchmark. Estimates of the MOC from models that most realistically represent the ocean are instead used as a ''true'' depiction of the MOC. Recent work by Farneti et al. (2015) and Downes and Hogg (2013) show that there is considerable spread in the strength of the MOC across coarse-resolution (1°) models forced with the Coordinated Ocean-Ice Reference Experiment, phase 2 (CORE-II), winds (Large and Yeager 2009) and among coupled climate models, respectively. Climate models rely on an accurate parameterization of mesoscale eddies, which are not routinely resolved in climate models (Gent and McWilliams 1990, hereinafter GM). Idealized studies show that the MOC response is more sensitive to model resolution than is the ACC transport (Stewart et al. 2014; Morrison and Hogg 2013).

To address how the MOC will respond to changing winds, a wide range of model experiments have been performed from idealized eddy-resolving zonally reentrant channels to more realistic coarse-resolution global circulation models. Gent (2016) provides an extensive review of the effects of Southern Hemisphere wind changes on the MOC in ocean models. Idealized studies that are eddy resolving show that there is partial eddy compensation, but results are sensitive to surface boundary conditions (Abernathey et al. 2011; Wolfe and Cessi 2010). Gent and Danabasoglu (2011, hereinafter GD11) show that in a realistic coupled climate model, eddy compensation is achieved if the GM eddy coefficient is allowed to vary in space and time in response to changes in stratification, which is consistent with idealized studies where EKE increases with winds (Abernathey et al. 2011; Morrison and Hogg 2013). The highest-resolution simulations to date to investigate MOC changes due to wind forcing are a Southern Hemispheric eddy-permitting model (1/6°; Hallberg and Gnanadesikan 2006) and a global eddy-permitting (1/4°) simulation (Treguier et al. 2010). However, both models are uncoupled to the atmosphere and representation of Southern Ocean mesoscale eddies might be underresolved, because the first baroclinic deformation

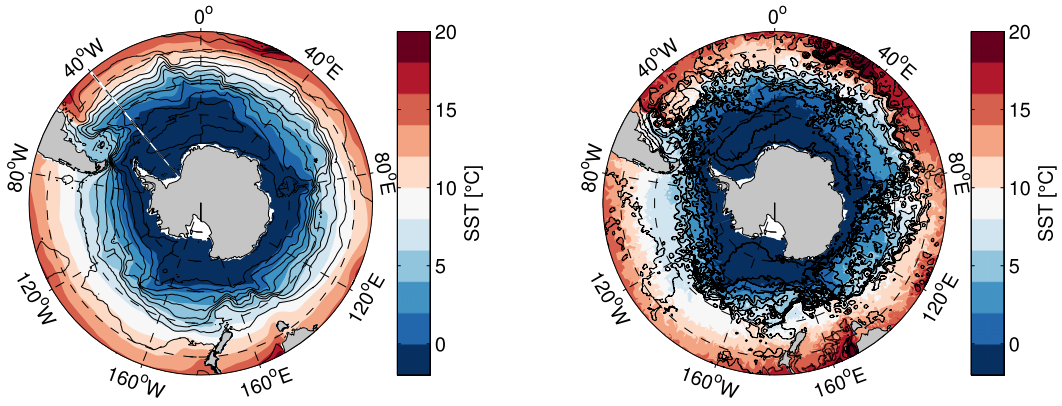

FIG. 1. Snapshots of austral winter SST and SSH in (left) low- (1°) and (right) high-resolution (0.1°) CESM. Color contours are SST [contour interval (ci) = 2°C] and black contours are SSH (ci = 25 cm).

radius, which is the characteristic spatial length scale of mesoscale eddies and ranges from 6 to 25 km in the Southern Ocean (Smith 2007), requires higher than 1/6° resolution south of 30°S (Hallberg 2013).

To overcome uncertainty regarding the parameterization and resolution of mesoscale eddies, this study examines the ACC transport and MOC response to changing winds in a new, high-resolution version of the Community Earth System Model (CESM). The experiment is conducted with a fully coupled configuration of CESM with an eddy-resolving (0.1°) ocean component and high-resolution (0.25°) atmosphere, which also includes sea ice and land components at the same resolution as the ocean and atmosphere, respectively. The increase in resolution compared to a standard CESM simulation at coarse resolution (1° ocean and atmosphere) can be seen from snapshots of sea surface temperature (SST) and sea surface height (SSH) in Fig. 1. When mesoscale eddies are explicitly resolved, there is more filamentary structure and closed contours of SSH.

With this high-resolution version of CESM, we test the ideas of eddy saturation and eddy compensation by running a 20-yr wind perturbation (WP) experiment in which the zonal wind stress in the Southern Ocean south of 30°S is increased by 50%, the same as the perturbation experiment PERT1 in GD11. This is the highest-resolution simulation brought to bear on this problem to date. A challenge of interpreting our results is that a 20-yr perturbation experiment will not have equilibrated in the deep ocean. Other modeling efforts at eddy-permitting resolution (0.25°) have experienced considerable model drift (Treguier et al. 2010). The emphasis of this study is on the transient response of the upper part of the ACC. However, the deeper ACC comes into play through the momentum budget. With this experiment being the first of its kind at this resolution, it is expected that these caveats will be refined over time. Model drift will be discussed further in the model description section.

One of the interesting results of this study is that standing eddies play the dominant role in the response of the MOC to increasing winds compared to transient eddies. Standing eddies were recognized as a major contributor to meridional fluxes in the Southern Ocean by early studies (de Szoeke and Levine 1981; Treguier and McWilliams 1990; Wolff et al. 1991). However, popular theoretical models of the ACC are framed in terms of a "streamwise average," which follows the meanders of the time-mean current, effectively eliminating the standing component and leaving a balance between a wind-driven Ekman component and a transient-eddy component (Marshall et al. 1993; Marshall and Radko 2003; Nikurashin and Vallis 2012). Recent studies have reemphasized the importance of standing eddies for the time-mean meridional flux of heat in the Southern Ocean (Volkov et al. 2010; Bryan et al. 2014) and in the response to wind perturbations (Dufour et al. 2012; Viebahn and Eden 2012; Zika et al. 2013b; Thompson and Garabato 2014; Abernathey and Cessi 2014).

Finally, we show that differences in surface buoyancy flux are closely tied to changes in the MOC. For example, increased upwelling of cold water can lead to cooler SSTs and consequently a decrease in latent and sensible heat fluxes. As described in the theoretical model of Marshall and Radko (2003), the net upwelling and subduction in and out of the surface layer must be balanced by diabatic processes (air–sea fluxes and mixing) within the surface layer. In an idealized, ocean-only, eddy-resolving model, Abernathey et al. (2011) showed how wind perturbation experiments could lead to different MOC changes depending on the details of the surface buoyancy boundary conditions. Only a coupled climate model, such as the one examined here, can hope to represent the full range of feedbacks that govern the

changes in SST, surface buoyancy flux, and MOC in response to a wind perturbation. In section 6, we examine the connection between changes in surface buoyancy flux and changes in overturning through the lens of water mass transformation.

The paper is organized as follows. In section 2 the MOC and its constituents are defined. In section 3 the control and WP experiments using high-resolution CESM are described. Section 4 shows the results of the ACC transport and MOC response in the WP experiment compared to the control simulation. Section 5 discusses the importance of the standing component of the mean overturning circulation in the MOC balance. Section 6 makes the connection between water mass modification and changes in the MOC. Last, section 7 contains a discussion and the conclusions of our results.

2. Meridional overturning circulation

The Southern Ocean MOC in depth space, referred to here as the Eulerian-mean MOC, is calculated by integrating the meridional velocity v zonally and vertically:

$$\psi(y,z) = \overline{\oint \int_z^0 v\, dz'\, dx}, \tag{1}$$

where x and z are the zonal and vertical coordinates, respectively. The overbar indicates a time average, $\overline{(\,)} \equiv (1/\tau)\int_0^\tau (\,)\, dt$, where τ is the averaging period. This representation of the MOC is largely made up of the wind-driven Ekman circulation that is well known as the Deacon cell. It was later realized by Döös and Webb (1994) that the Deacon cell vanishes when the MOC is calculated vertically in density rather than depth space. The overturning circulation calculated in density space better represents water mass transport, which is largely along isopycnals in the ACC interior and consistent with the net overturning resulting from two opposing mechanisms: the wind-driven circulation of the Deacon cell and the eddy-driven circulation. The MOC is defined as

$$\psi_{\rm moc}(y,\sigma) = \overline{\oint \int_\sigma^{\sigma_s} v h\, d\sigma'\, dx}, \tag{2}$$

where $h(x, y, \sigma, t) \equiv -\partial\tilde{z}/\partial\sigma$ is the thickness of isopycnal layers, $\tilde{z}$ is the depth of isopycnal surfaces, and σ_s is the density value at the surface. The variable σ is potential density, and in practice σ_2 (potential density referenced to 2000 m depth) is used to calculate the MOC since its vertical structure tends to have monotonic profiles and is a good representation of the MOC calculated in neutral density classes (Lee and Coward 2003). As mentioned above, $\psi_{\rm moc}$ can be thought of as consisting of two opposing cells between the wind-driven overturning circulation $\overline{\psi}$ and transient-eddy-induced overturning circulation ψ^*:

$$\psi_{\rm moc}(y,\sigma) = \overline{\psi} + \psi^*. \tag{3}$$

The time-mean overturning circulation in isopycnal coordinates is defined as

$$\overline{\psi}(y,\sigma) = \oint \int_{\overline{\sigma}}^{\overline{\sigma}_s} \overline{v}\,\overline{h}\, d\sigma'\, dx, \tag{4}$$

where $\overline{h}(x, y, \sigma)$ is the time-mean thickness of isopycnal layers. The transient-eddy-induced overturning circulation is then given by the difference between the MOC and time-mean streamfunctions as

$$\psi^*(y,\sigma) = \psi_{\rm moc} - \overline{\psi} = \overline{\oint \int_\sigma^{\sigma_s} v' h'\, d\sigma'\, dx}, \tag{5}$$

where the prime indicates a deviation from the time mean.

3. Model

a. Control experiment

The model used in this study is a high-resolution version of the CESM (Hurrell et al. 2013), a new-generation climate system model that is the successor to the Community Climate System Model, version 4 (CCSM4; Gent et al. 2011). Details of the simulation examined are summarized below, but for a more in-depth description, see Small et al. (2014). The model configuration includes the Community Atmosphere Model, version 5 (CAM5), with a spectral element dynamical core; Community Ice Code, version 4 (Hunke and Lipscomb 2008); Parallel Ocean Program, version 2 (POP2); and Community Land Model, version 4 (Lawrence et al. 2011). CAM5 was integrated with a horizontal resolution of about 0.25° (specifically, the spectral element dynamical core with 120 elements on each face of the cubed sphere, referred to as ne120) and 30 levels in the vertical.

The POP2 model has a nominal grid spacing of 0.1° (decreasing from 11 km at the equator to 2.5 km at high latitudes) on a tripole grid with poles in North America and Asia. The configuration is similar to that used in McClean et al. (2011) and Kirtman et al. (2012), except that the number of vertical levels was increased from 42 to 62, with more levels in the main thermocline. The ocean communicated with the coupler, providing updated SST and surface currents and receiving updated surface fluxes, every 6 h, and the atmosphere communicated every 10 min. The coupler computes air–sea fluxes using the

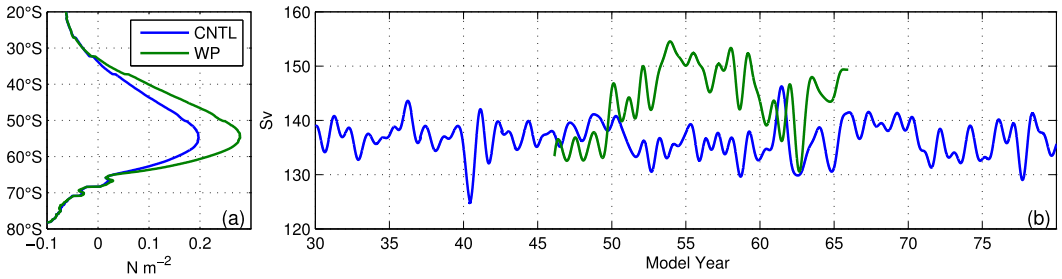

FIG. 2. (a) Time- and zonal-mean zonal wind stress for the control (CNTL) and WP experiments for model years 56–66. (b) One-year low-pass filtered times series of Drake Passage transport using a fourth-order Butterworth filter centered around model years 45–66. The first and last year of each time series was removed because of Gibbs ringing at the end points.

Large and Yeager (2009) surface layer scheme. The land and sea ice models are on the same grids as the atmosphere and ocean models, respectively. POP2 has been shown to produce eddy covariances consistent with observations in the Pacific (Bishop and Bryan 2013) and Southern Ocean (Lenn et al. 2011), and this high-resolution version of CESM through spectral analysis produces mesoscale eddy covariances of SST and geostrophic meridional velocity that are consistent with satellite observations (Abernathey and Wortham 2015).

Following a 15-yr spinup, the model was run for 86 years. We will refer to the last 86 years with model year 1 being equivalent to aggregate simulation year 16. For the current work we will focus on model years 45–66, which are the years when the WP experiment was performed and is described below. This time period was chosen because surface fluxes and ACC transport through Drake Passage had reached equilibrium by model year 45 (Small et al. 2014).

b. *Wind perturbation experiment*

The WP experiment is conducted with the same methodology as the PERT1 experiment in GD11 where the Southern Hemisphere zonal wind stress is increased by 50%, but here using CESM rather than CCSM4. The WP experiment is just short of a 21-yr simulation, starting from March of model year 45 of the control simulation to the end of model year 65. The WP experiment was conducted by multiplying the zonal wind stress, forcing the ocean component by 1.5 south of 35°S, with this factor linearly reducing to 1 to the north between 35° and 25°S and to the south between 65° and 70°S. The maximum time- and zonal-mean Southern Hemisphere wind stress is 41% larger compared with the control for model years 56–66, with an increase of $0.083\,\mathrm{N\,m^{-2}}$ from $0.197\,\mathrm{N\,m^{-2}}$ in the control to $0.280\,\mathrm{N\,m^{-2}}$ in WP (Fig. 2a), which is very close to the maximum wind stress values cited in GD11. The increased zonal wind stress was not used in the bulk formulae to calculate the atmosphere-to-ocean heat and freshwater fluxes, and the increased zonal stress is not felt directly by the atmosphere component.

One of the complications of interpreting a perturbation experiment is model drift. As mentioned before, model drift complicated results in lower-resolution studies (Treguier et al. 2010). The shortness of our WP experiment was dictated by very high computational costs. As demonstrated in Small et al. (2014) and in Fig. 2b, ACC transport through Drake Passage is in equilibrium in the control, exhibiting mainly interannual variability. After a decade of the WP simulation, surface variables reached a new equilibrium, which is demonstrated in surface EKE in Fig. 4 and described in the next section. However, deep variables have not reached a new equilibrium. Figure 3 shows the monthly averaged and area-averaged deep ocean temperature for the Southern Ocean in the control and WP. The control deep ocean temperature is in equilibrium, albeit with some decadal variability, but the WP is not. The integration needs to be longer for the deep ocean to come to equilibrium.

4. Results

a. *ACC transport response*

The ACC transport through Drake Passage is shown in Fig. 2b. The mean and standard deviation for the

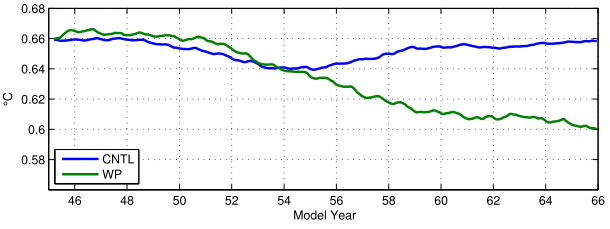

FIG. 3. Southern Ocean monthly time-averaged and area-averaged (south of 30°S) ocean temperature at 2889 m depth for the CNTL and WP simulations.

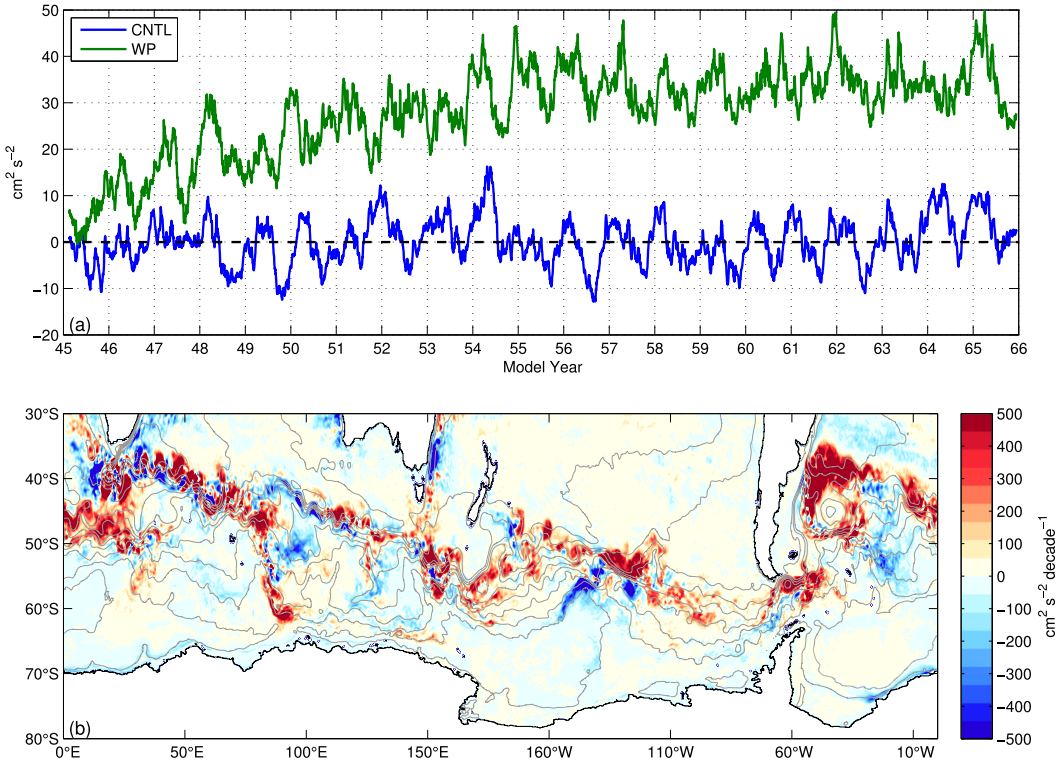

FIG. 4. (a) Area-averaged time series of daily surface EKE anomaly referenced to the control mean derived from daily SSH. (b) The 10-yr linear trend in EKE for model years 45–56 in the WP experiment (color contours, ci = 50 cm^2 s^{-2} decade^{-1}). For reference to the ACC, light gray contours are the mean SSH (ci = 25 cm) for the WP experiment.

control and WP are 136 ± 3 Sverdrups (Sv; 1 Sv ≡ 10^6 m^3 s^{-1}) and 144 ± 6 Sv, respectively. The WP time series has a trend over the first 10 years of 23 Sv decade^{-1}, with a small negative trend over the last 10 years of −6 Sv decade^{-1}. It is not immediately clear why there is a small negative trend over the remaining 10 years. The overall WP mean transport only increases by 6%, with a 41% increase in the zonal wind stress compared to the control simulation. These results suggest that the ACC transport is largely eddy saturated.

The area-averaged surface EKE south of 30°S increased immediately following the change in wind stress and then continued to increase for a period of 10 years, before stabilizing at a value 28% higher than the control mean (Fig. 4a). The area-averaged surface EKE has a linear trend over the first 10 years of 26 cm^2 s^{-2} decade^{-1}, but no trend in the last 10 years. However, the spatial distribution of the EKE trends over the first 10 years have positive and negative values that are $O(\pm 100)$ cm^2 s^{-2} decade^{-1} (Fig. 4b), resembling the mean EKE difference over the last 10 years of the simulation (Fig. 5). Figure 5 shows that there are both regions of enhancement and suppression of EKE along the mean path of the ACC with increased zonal wind stress. Outside of the Malvinas and the Agulhas return flows, the positive trends are largely in regions where standing meanders of the mean flow occur in the lee of major topographic features, as shown in Thompson and Garabato (2014) and Abernathey and Cessi (2014). Both the ACC transport through Drake Passage and the area-averaged EKE have a linear trend during the first 10 years of the WP (Fig. 2b). Once the area-averaged EKE reaches an asymptote of ~35 cm^2 s^{-2} above the control mean, the ACC transport adjusts to the elevated EKE. For this reason, overturning streamfunctions are calculated for the final 10 years of the WP experiment (model years 56–66) in the next section.

The small increase in ACC transport is also reflected in the differences in isopycnal surfaces between simulations (Fig. 6). The differences are largely focused in the upper ocean, in particular, the top 100 m within the mixed layer (Fig. 6b). There are only small changes in the interior (Fig. 6a). The top 100 m is characterized by an increase in surface density in WP as compared to the control (Figs. 11a,b). There is also lighter (or more buoyant) waters at depth north of 45°S. This represents a surface-intensified steepening of isopycnal surfaces, which makes up the increase in the ACC transport. On

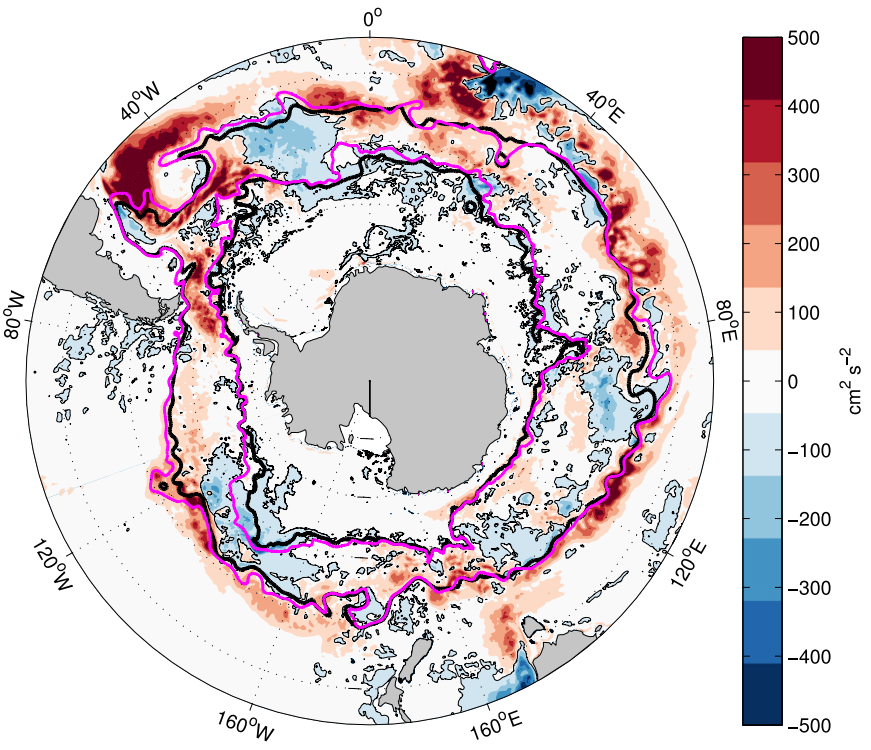

FIG. 5. Change in upper 1000 m vertically averaged EKE (WP minus control) for model years 56–66. Color contours have ci = 100 cm^2 s^{-2} and thin black contours are where the change in EKE is zero. The thick black (control) and magenta (WP) contours are the −150- and −25-cm mean SSH contours that pass through Drake Passage.

average, the water is denser with a skewed probability density distribution (Fig. 6c).

b. *MOC response*

1) EULERIAN-MEAN MOC

The mean overturning streamfunction is made up of the clockwise (looking west) wind-driven circulation in depth–latitude space, the Deacon cell, and a weaker counterclockwise circulating lower cell (Fig. 7). As expected with the increased winds in the WP simulation, the Deacon cell is intensified. The peak values of the Deacon cell are 40.5 and 57.1 Sv in the control and WP, respectively (Figs. 7a,b). The latitude and depth of the maximum values of the Deacon cell are similar between simulations. The latitude and depth of the maximum

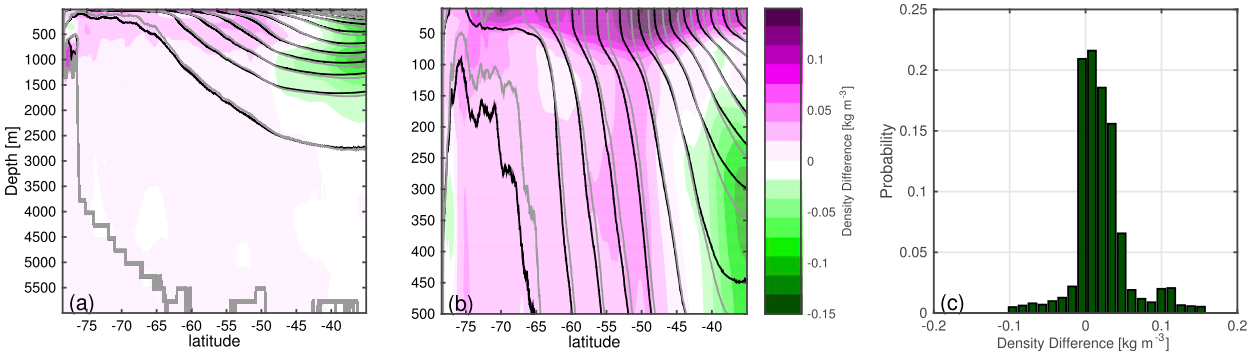

FIG. 6. Differences between the time- and zonal-mean σ_2 (WP minus control) for model years 56–66. (a) Full water column. Color contours are the differences with ci = 0.02 kg m^{-3}. (b) As in (a), but for the upper ocean. The black and gray contours in both are the depth of the time- and zonal-mean σ_2 surfaces in the control and WP simulations, respectively, with ci = 0.25 kg m^{-3}. (c) Probability density distribution for potential density differences.

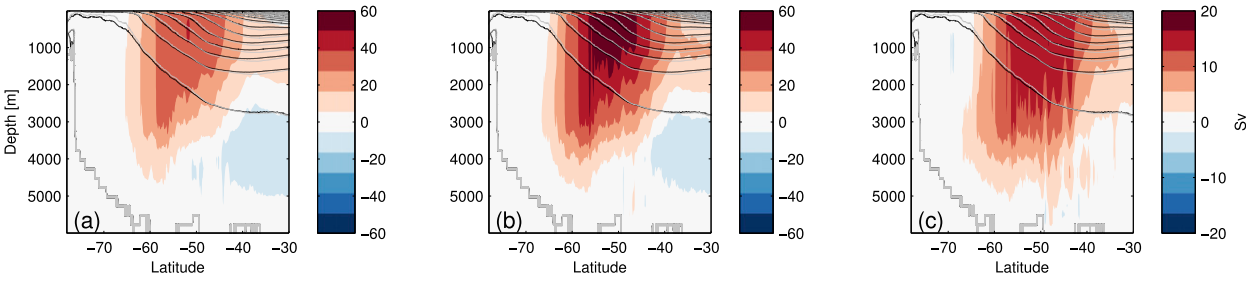

FIG. 7. The Eulerian-mean MOC [Eq. (1)] for the (a) control, (b) WP, and (c) difference. The color contours are the overturning streamfunction (Sv) with ci = 10 Sv for (a) and (b) and ci = 4 Sv for (c). The black and gray contours are the depth of the time- and zonal-mean σ_2 surfaces in the control and WP simulations, respectively, with ci = 0.25 kg m^{-3}.

value of the Deacon cell in the control simulation is 51.8°S and 607 m, respectively (Fig. 7a). In WP they are 51.6°S and 552 m, respectively (Fig. 7b). The maximum increase in the Deacon cell between the control and WP is 17 Sv and occurs at 48.3°S and at 830 m depth. This is equivalent to a 41% increase in transport, consistent with a linear relationship with the surface wind stress (Fig. 7c).

The lower cell is reduced slightly between the control and WP (Fig. 7c). The maximum values of the lower-cell circulation are −14.7 Sv and −13.5 Sv in the control and WP respectively. The latitude and depth of the maximum value of the lower cell in the control simulation is 36.9°S and 3752 m respectively (Fig. 7a). In WP they are 36.6°S and 3752 m respectively (Fig. 7b).

2) MERIDIONAL OVERTURNING CIRCULATION

The overturning streamfunction in isopycnal coordinates, referred to as the MOC, is estimated in this section for the control and WP experiments. Comparing the diagnosed MOC [Eq. (2)] against a schematic of the overturning [Fig. 18 in Farneti et al. (2015)] there are four distinct circulation cells, but there are only two cells that change substantially between our simulations, which will be described (Figs. 8a–c). There is a clockwise-rotating (looking west) upper cell centered at 48.1°S and 36.2σ_2, with a maximum of 19.8 Sv in the control (Fig. 8a). The upper cell in WP is centered at 48°S and 36.35σ_2 with a maximum of 27.5 Sv (Fig. 8b). The upper cell increased by a maximum of 7.7 Sv, which is a 39% increase over the control (Fig. 8c).

There is a counterclockwise-rotating cell called the lower cell that has an enhanced poleward region with a maximum of −20 Sv at 63.5°S and 37.15σ_2 in the control (Fig. 8a). In WP the lower cell has a maximum of −32.7 Sv at 64°S and 37.15σ_2 (Fig. 8b). The counter circulation of the lower cell increased by a maximum of 12.6 Sv in WP compared with the control, which is a 64% increase over the control (Fig. 8c). The lower cell equatorward of 50°S has no difference between simulations (Fig. 8c).

One decomposition of the MOC is between the time-mean overturning [Eq. (4)] and the transient-eddy-induced overturning [Eq. (5)] as stated in Eq. (3). The time-mean overturning streamfunction (Figs. 8d–f) has a nearly identical structure of circulation cells to the MOC (Figs. 8a–c). The upper cell has a clockwise circulation with a maximum of 22.3 Sv at 52.2°S and 36.45σ_2 in the control (Fig. 8d). In WP the mean upper cell has a maximum of 30.7 Sv at 48.3°S and 36.30σ_2 (Fig. 8e). The difference in the maximum values of the upper cell is 8.4 Sv, which is a 38% increase over the control simulation (Fig. 8f). The lower cell has as a maximum value of −19.6 Sv at 64.5°S and 37.15σ_2 in the control (Fig. 8d). In WP it has a maximum value of −30.9 Sv at 65.2°S and 37.15σ_2 (Fig. 8e). The lower cell increases by 11.3 Sv, which is 58% greater than the control (Fig. 8f).

The transient-eddy-induced streamfunction has a different structure than the MOC or the mean overturning (Figs. 8g–i). There are two counter-circulating cells: an upper and a deep cell. The upper cell is the stronger of the two and has a maximum of −16.7 Sv at 43.7°S and 35.30σ_2 for the control (Fig. 8g). The upper cell in WP has a maximum of −20.5 Sv at 43.4°S and 35.30σ_2 (Fig. 8h). The small differences between the two simulations are at most ±5 Sv concentrated in the upper cell with virtually no change between the lower cells (Fig. 8i). Overall, the transient-eddy component does not make a large contribution to the zonal-mean overturning, as seen also in Dufour et al. (2012). However, an analysis in streamwise coordinates (not performed here) would likely find a much greater role for transient eddies (Viebahn and Eden 2012; Abernathey and Cessi 2014).

5. Time-mean meridional overturning streamfunction

In the previous section, it was shown that little or no eddy compensation is apparent when the MOC is decomposed into time-mean and transient components. Much of the change in the MOC is reflected in the

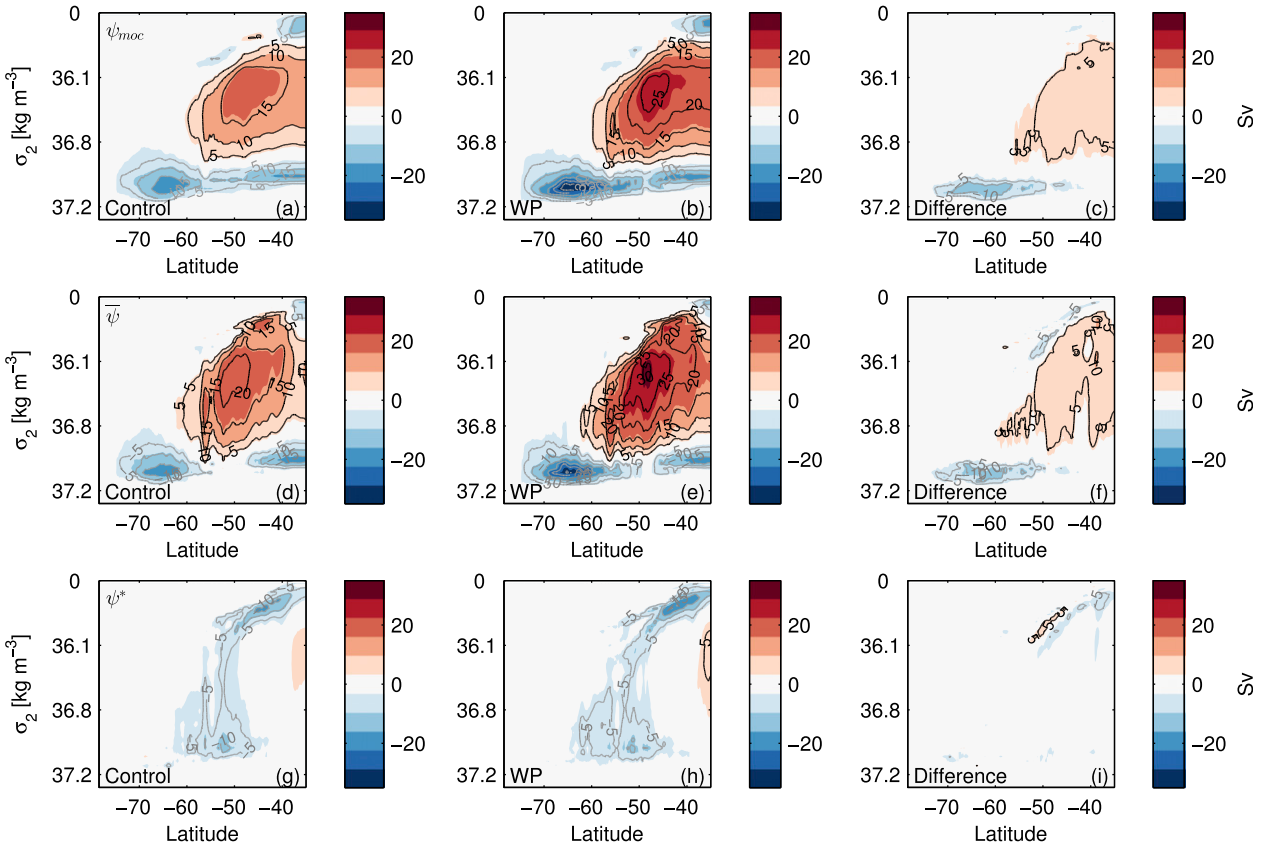

FIG. 8. (a)–(c) MOC (ψ_{moc}), (d)–(f) mean overturning circulation ($\overline{\psi}$), and (g)–(i) transient-eddy overturning circulation (ψ^*) for the (left) control, (middle) WP, and (right) difference (WP minus control). Color contours have ci = 6 Sv. Black and gray contours are positive and negative overturning circulation, respectively, with ci = 5 Sv.

time-mean MOC (Figs. 8c,f). This prompted further investigation into the time-mean overturning streamfunction. The time-mean overturning circulation $\overline{\psi}$ can be decomposed into a time- and zonal-mean streamfunction $[\overline{\psi}]$ and a deviation from the zonal mean as the "standing" component $\psi^\dagger$,

$$\overline{\psi} = [\overline{\psi}] + \psi^\dagger . \tag{6}$$

The term $[\overline{\psi}]$ is defined as

$$[\overline{\psi}](y,\sigma) = \oint \int_{[\overline{\sigma}]}^{[\overline{\sigma}_s]} [\overline{v}][\overline{h}]\, d\sigma'\, dx , \tag{7}$$

where [ ] is a zonal average, $[\,] \equiv [1/L(y)] \oint (\,)\, dx$, and $L(y)$ is the circumpolar length of a given latitude circle. The residual overturning streamfunction is finally written as the three-part balance

$$\psi_{\text{moc}} = [\overline{\psi}] + \psi^\dagger + \psi^* . \tag{8}$$

The time- and zonal-mean component is essentially the Eulerian-mean MOC (Fig. 7) and remapped to the time- and zonal-mean depth of σ_2 surfaces (Figs. 9d–f). The differences in circulation cells then are equivalent to the values stated for the Deacon cell and lower cell in section 4b. This decomposition is more physically insightful, because $[\overline{\psi}]$ is directly proportional to the zonal-mean Ekman transport and is therefore clearly wind driven.

The standing component of the MOC is shown in Figs. 9g–i. Similar to the transient component, it has two counter cells that are comparable in strength: an upper and a lower cell. However, the standing component is stronger than the time- and zonal-mean component. The upper cell has a maximum of −39.9 Sv at 51.5°S and 35.8σ_2 in the control (Fig. 9g). The upper cell in WP has a maximum of −54.7 Sv at 51.1°S and 35.9σ_2 (Fig. 9h). The upper cell increased by 14.8 Sv, which is 37% over the control (Fig. 9i).

The lower cell of the standing component has a maximum of −39.1 Sv at 57.8°S and 37.1σ_2 in the control (Fig. 9g). In WP the maximum is −61.8 Sv at 57.8°S and 37.12σ_2 (Fig. 9h). There is a 22.7 Sv increase in the lower-cell circulation, which is a 58% increase over the control (Fig. 9i).

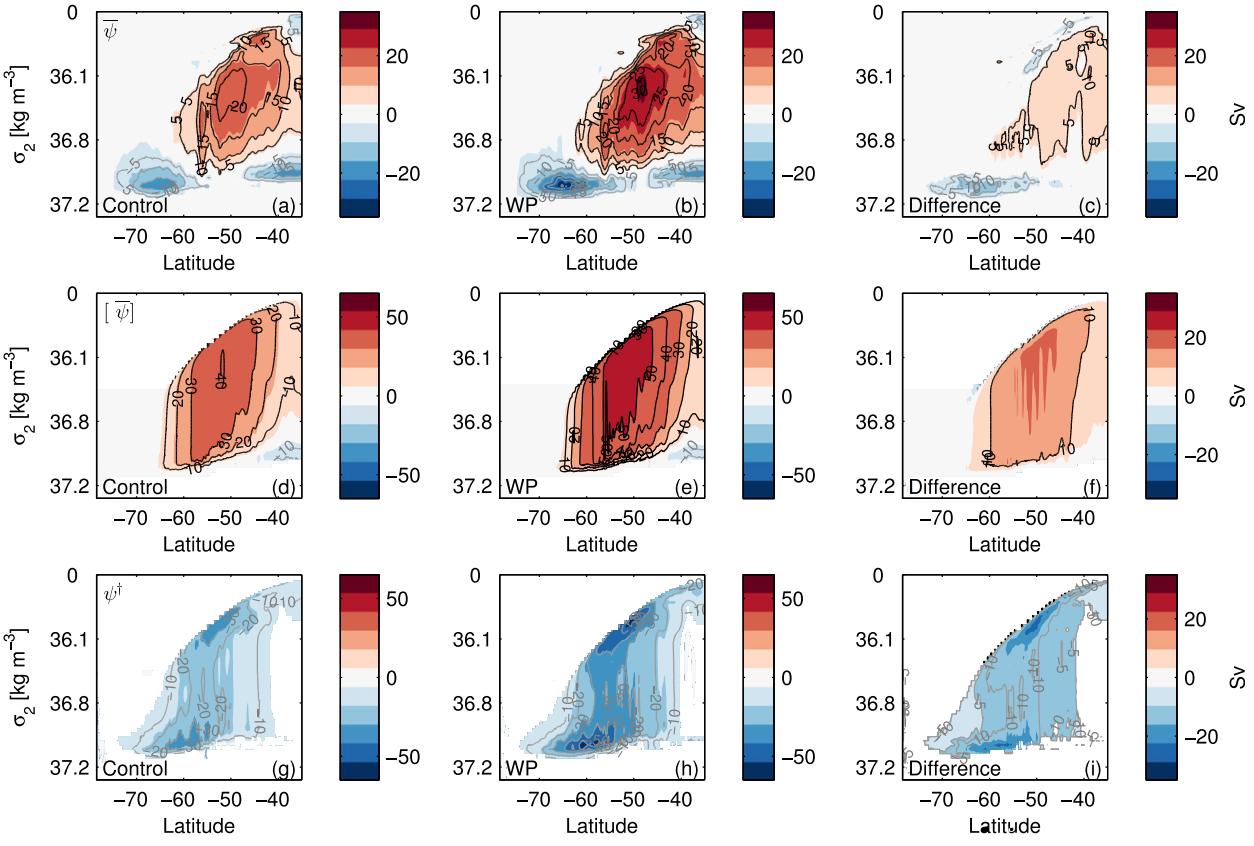

FIG. 9. Mean overturning circulation $\overline{\psi}$ decomposed into the time- and zonal-mean $[\overline{\psi}]$ and standing $\psi^{\dagger}$ overturning circulation. (a)–(c) Mean overturning (same images as Figs. 8d–f), (d)–(f) time- and zonal-mean overturning, and (g)–(i) standing overturning circulation for the (left) control, (middle) WP, and (right) difference (WP minus control). Color contour levels have ci = 6 Sv except (d),(e),(g),(h), which have ci = 12 Sv. Black and gray contours are positive and negative overturning circulation, respectively, with ci = 5 Sv.

A large degree of compensation exists between the wind-driven time- and zonal-mean cell and the standing component of the overturning circulation, even though the peaks in overturning do not coincide in density–latitude space. In both the control experiment and in response to the wind perturbation,

$$\delta\psi_{\text{moc}} \approx \delta[\overline{\psi}] + \delta\psi^{\dagger}, \tag{9}$$

since the change in transient-eddy overturning is negligible, $\delta\psi^{*} \approx 0$ (Fig. 8i). The variable δ here means WP minus the control experiment. It is interesting to note that the lower cell does not exist in the time- and zonal-mean component of the overturning (Figs. 9d–f). It is only through the standing component of the overturning that the lower cell exists in our simulations (Figs. 9g–i).

The time-mean kinetic energy $\overline{K} = (1/2)(\overline{u}^2 + \overline{v}^2)$ is also dominated by the standing component, which reflects changes in the zonal distribution of kinetic energy. The time-mean kinetic energy is decomposed into a time- and zonal-mean component and a standing component,

$$[\overline{K}] = \underbrace{\frac{1}{2}([\overline{u}]^2 + [\overline{v}]^2)}_{\text{Mean}} + \underbrace{\frac{1}{2}([u^{\dagger 2}] + [v^{\dagger 2}])}_{\text{Standing}}. \tag{10}$$

The biggest changes in the kinetic energy are in the standing component (Fig. 10). The longitudinal changes in the velocity field enhances mean kinetic energy as baroclinic eddy growth rates respond to changes in mean stratification and vertical shear (Thompson and Garabato 2014).

6. Surface water mass transformation

Analysis of changes in the surface water mass transformation is used to better understand the thermodynamics of the changes in the MOC. Here "water mass transformation" refers to the thermodynamic modification of water density due to diabatic processes such as surface buoyancy fluxes and mixing. When the transformation rates are integrated over isopycnals in an ocean basin, the net transformation must balance the inflow/outflow in density coordinates, that is, the MOC

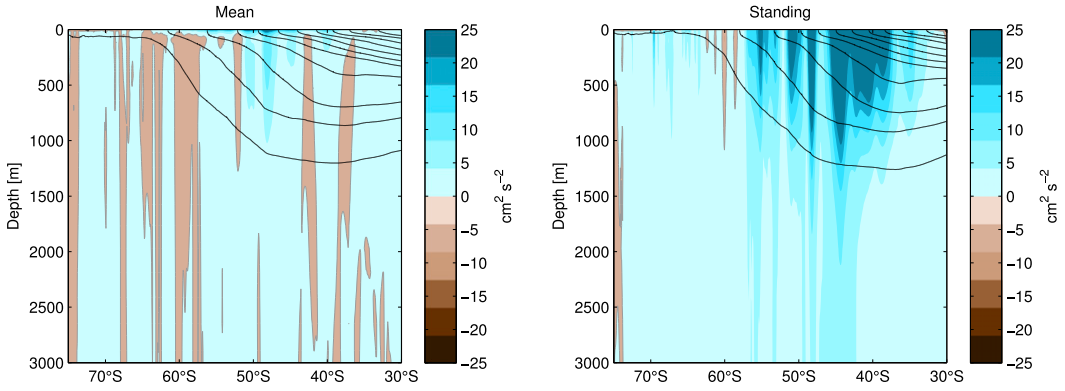

FIG. 10. The change in the time- and zonal-mean kinetic energy [Eq. (10)] between the WP and control simulations for model years 56–66.

defined in Eq. (2) (Walin 1982; Tziperman 1986; Speer and Tziperman 1992; Marshall et al. 1999; Marsh et al. 2000; Large and Nurser 2001; Iudicone et al. 2008; Downes et al. 2011). We can therefore expect the changes in Eq. (2) under wind perturbation to be accompanied by changes in water mass transformation rates.

With the wind perturbation there is an indirect effect on the coupled system through changes to the surface properties, and this is reflected in changes to the net surface buoyancy flux ($\mathscr{B}$). Mean changes in density, SST, and sea surface salinity (SSS) are shown in Fig. 11. Surface density increases almost uniformly along the ACC, with smaller patches of lighter waters found north of 45°S (Fig. 11a). The zonally averaged density distribution shows that the surface waters are denser at all latitudes except near 30°S and the increase peaks near 50°S (Fig. 11b). The changes in SST and SSS reflect this increase in density. Water spanning 10°–20° latitude surrounding Antarctica are warmer and saltier by as much as 1°–2°C and 0.25–0.5 g kg^{-1}, respectively (Figs. 11c,e). The warmer and saltier waters around Antarctica are mostly density compensated, but density does increase slightly. Water is cooler throughout most of the Pacific and Indian Oceans, but salinity changes are less prominent, with the exception that water is fresher near 30°S in the Pacific. The zonally averaged SST and SSS show that the surface waters are saltier at latitudes south of 30° (Fig. 11f), but zonal-average SST is only warmer south of 50°S (Fig. 11d).

Changes in the surface density field reflect changes to the surface buoyancy flux between the simulations shown in Fig. 12. Surface buoyancy flux is the sum of surface heat flux (Q_o) and freshwater flux (FWF),

$$\mathscr{B} = \frac{\alpha_\theta g}{\rho_o c_p} Q_o - \frac{\alpha_S g}{\rho_{\rm fw}} S_o (E - P - R), \tag{11}$$

where $\alpha_\theta = \partial\sigma/\partial\theta$, θ is potential temperature, $\alpha_S = \partial\sigma/\partial S$ and S is salinity, $E - P - R$ is the surface FWF (evaporation minus precipitation minus runoff), g is the acceleration due to gravity, $\rho_o = 1026\,\text{kg m}^{-3}$ is the ocean reference density, $c_p = 3996\,\text{J kg}^{-1}\,\text{K}^{-1}$ is the specific heat at constant pressure for seawater, $S_o = 34.7\,\text{g kg}^{-1}$ is the ocean reference salinity for the virtual salt flux, and $\rho_{\rm fw} = 1000\,\text{kg m}^{-3}$ is the density of freshwater. The change in $\mathscr{B}$ shows a complex spatial pattern with a net buoyancy flux reduction near the coast of Antarctica and along the southern fringes of the subtropical gyres. Along the core of the ACC, patches of both increased and decreased surface buoyancy flux occur (Fig. 12a). The sign convention is such that negative buoyancy flux means the ocean is either cooling or becoming saltier. The zonally averaged $\mathscr{B}$ has sinusoidal meridional structure (Fig. 12b). The changes in surface heat flux (Fig. 12c) dominate changes in surface buoyancy forcing compared with FWFs (Fig. 12e). The FWF spatial difference (Fig. 12e) and zonal-average difference (Fig. 12f) both show positive buoyancy forcing near Antarctica. This is consistent with a reduction in sea ice in the WP simulation (Fig. 13). In austral summer [January–March (JFM)] and winter [July–September (JAS)], there is an overwhelming reduction in sea ice thickness surrounding Antarctica in the WP simulation. Changes in FWFs around Antarctica, though, are masked by increased surface heat fluxes.

Since the MOC was analyzed in σ_2 coordinates, we use the same coordinate for the water mass analysis. To calculate the time-mean surface water mass transformation, the surface buoyancy flux [Eq. (11)] is integrated over the surface outcrop area as

$$\Omega(\sigma_2) = \frac{1}{g}\frac{\partial}{\partial\sigma_2}\overline{\int_{\mathcal{A}_{\sigma_2}} \mathscr{B}\, dA}, \tag{12}$$

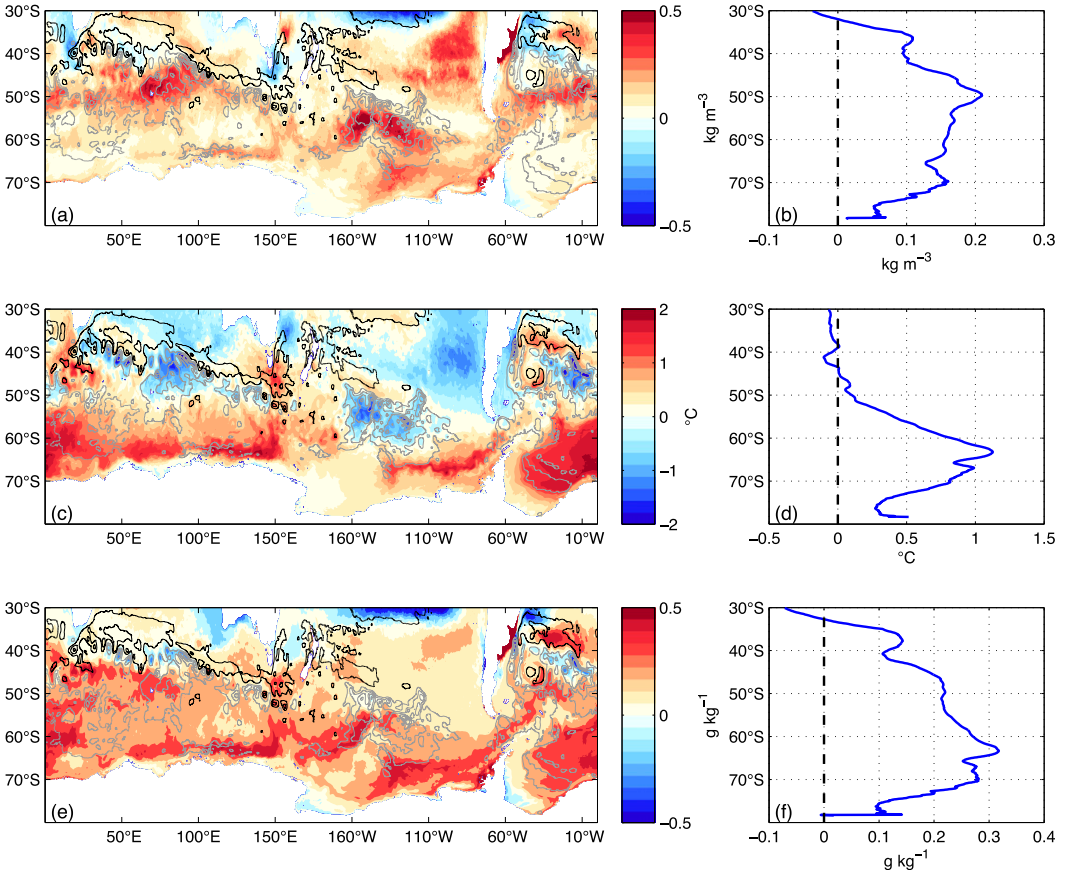

FIG. 11. Sea surface density, temperature, and salinity differences (WP minus control) for model years 56–66. (a) Density difference (color contours, ci = 0.06 kg m^{-3}), (b) zonal-average surface density, (c) SST color contours (ci = 0.2°C), (d) zonal-average SST, (e) salinity differences (ci = 0.06 g kg^{-1}), and (f) zonal-average salinity. Black (positive) and gray (negative) contours (ci = 10 cm) are the change in mean SSH.

where $\mathcal{A}_{\sigma_2}$ represents integration over the area south of 30° S with density greater than σ_2. By breaking $\mathscr{B}$ into Q_o and FWF components, Ω can be decomposed into transformation due to Q_o ($\Omega_{\rm HF}$) and FWF ($\Omega_{\rm FWF}$). There are additional contributions to water mass transformation due to interior mixing and cabbeling, but those are not diagnosed here (the necessary model output was not saved). As shown below, changes in surface transformation can explain most of the changes in the MOC.

Figure 14 shows the annual mean Ω, $\Omega_{\rm HF}$, and $\Omega_{\rm FWF}$ for both control and perturbation experiments. Examining the control case first, we see that Ω contains three peaks, each corresponding with one of the cells of $\psi_{\rm moc}$ described above and shown in Fig. 8. (The transformation rates should be compared with the MOC at 30°S.) For the densest waters ($36.6 < \sigma_2 < 37.2\,{\rm kg\,m^{-3}}$) surface cooling makes water denser, with a peak transformation rate of 14 Sv; this corresponds with the lower cell of the MOC. For water of intermediate density ($35.4 < \sigma_2 < 36.5\,{\rm kg\,m^{-3}}$), a combination of heat and FWFs (the dominant component) makes the water lighter, with a peak transformation rate of −32 Sv; this corresponds with the upper cell of the MOC. The quantities Ω and $\psi_{\rm moc}$ do not match up perfectly, since we have not calculated the transformation due to mixing; however, this component can be inferred as the residual, as shown in Newsom et al. (2016). Mixing causes additional water to be entrained into the subpolar cell; in contrast, mixing weakens the upper cell slightly and redistributes its position in density space.

The WP experiment produced a strengthening of both the upper and lower MOC cells. Correspondingly, in Fig. 14 we see that the transformation rates associated with these cells also increase in magnitude. The increased heat loss associated with the lower cell causes transformation to nearly double for water denser than $\sigma_2 = 37.0\,{\rm kg\,m^{-3}}$, to a maximum of 26 Sv, matching the 12-Sv increase in overturning almost exactly. Although

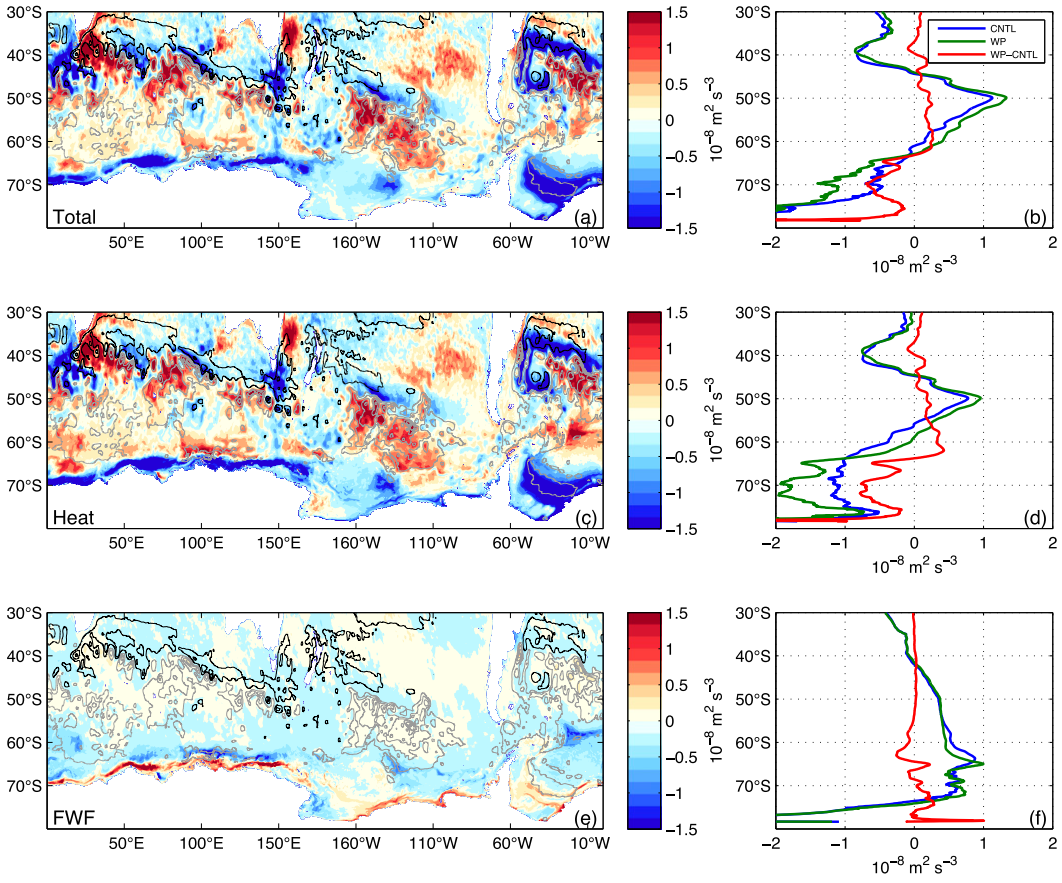

FIG. 12. Surface buoyancy flux differences between the control and WP experiments for model years 56–66. The sign convention of negative means the ocean is cooling or becoming saltier. (a) Total surface buoyancy and contributions from (c) heat and (e) freshwater fluxes (ci = 0.15×10^{-8} m^2 s^{-3}). (b),(d),(f) The zonally averaged total surface buoyancy, heat, and freshwater flux contributions, respectively. Black (positive) and gray (negative) contours (ci = 10 cm) are the change in mean SSH.

the upper cell transformation is dominated by FWFs in the control, it is the heat fluxes that change most strongly under the WP; increased density gain due to surface heat flux strengthens the upper-cell transformation to nearly −40 Sv and shifts its maximum from $\sigma_2 = 36.0$ to $\sigma_2 = 36.2$ kg m^{-3}, again consistent with the 8-Sv increase in the upper cell. Changes in transformation due to FWF changes were minimal, as also found by Newsom et al. (2016) in a greenhouse-warming scenario.

The changes in transformation are driven by the changes in heat flux shown in Fig. 12, namely, increased heat flux into the ocean in the ACC latitudes and increased heat flux out of the ocean near Antarctica. The physical explanation for this change is consistent with increased Ekman upwelling. In the ACC latitudes, where the water column is stably stratified in temperature, this brings cooler water to the surface and, because of the interactive nature of latent and sensible heat flux, produces increased heat gain. In the subantarctic region, where warmer water lies below the surface, increased upwelling has the opposite effect, producing increased heat loss. Overall, the entire pattern of Southern Ocean circulation and water mass transformation strengthens with increasing winds.

7. Discussion and conclusions

The Southern Ocean ACC transport and MOC response to changes in wind forcing in a fully coupled high-resolution climate model (CESM) are diagnosed. Results from a ~21-yr wind perturbation experiment, where the Southern Hemisphere winds were increased by 50%, show that the ACC transport is nearly eddy saturated, but the MOC is not eddy compensated. The ACC transport response through Drake Passage only changes marginally. During the first 10 years of the simulation, while the eddies are ramping up, the ACC transport has a linear trend of 23 Sv decade^{-1} in response to the increased wind forcing. After a decade the eddies have reached an equilibrium state and the ACC

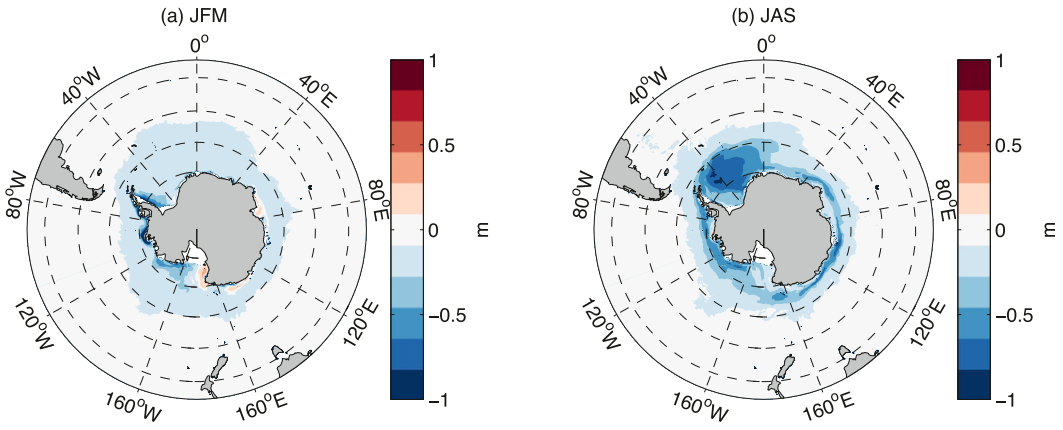

FIG. 13. Sea ice thickness difference (WP minus control) for model years 56–66. (a) JFM and (b) JAS difference (ci = 0.2 m).

transport adjusted to the elevated level of EKE. The overall ACC transport only increased by 6% compared to the control simulation, suggesting that the ACC is nearly eddy saturated. Recent studies have pointed to coastal winds near Antarctica as possible drivers of ACC transport variability (Zika et al. 2013a; Langlais et al. 2015), but the time- and zonally averaged wind in the WP experiment is indistinguishable from the control near the Antarctica coast south of 65°S (Fig. 2). Thus, these potential mechanisms for ACC transport variability are not explored in this paper.

The MOC increased in the upper and lower cells by 63% and 39%, respectively. When the MOC is decomposed into time-mean and transient-eddy contributions, the eddy-driven overturning does not change much compared to the control. This result is consistent with the mean upper-ocean EKE difference (Fig. 5), where EKE is enhanced and suppressed along the mean path of the ACC. The zonally integrated mean EKE difference sums to near zero, which may help to explain why our transient overturning difference is negligible. EKE is enhanced at choke points along the mean ACC path near major topography and in the western boundary current regions without any systematic shifts in the Southern Ocean SSH fronts.

Comparing the MOC results of this study with the same WP experiment (PERT1) performed in the coarse-resolution CCSM4 climate model in GD11, we find a lesser role for transient eddies. The biggest changes in the overturning circulation in our high-resolution experiment arise from enhancement of the steady rather than the transient-eddy-induced overturning. When the time-mean overturning circulation is decomposed into a time- and zonal-mean component and a standing component, the balance of the MOC is approximately between these two components [Eq. (9)]. As the winds increase, the standing component of the overturning acts to partially, but not perfectly, compensate for the increase in the wind-driven Deacon cell. We now see a potential role for another type of eddy, the standing eddy, at higher resolution than Hallberg and Gnanadesikan (2006), that plays the dominant role in poleward flow rather than transient eddies (Dufour et al. 2012) to counter the wind-driven equatorward circulation.

In a coupled model, changes in the MOC are connected directly with changes in surface water mass transformation. This is because of changes in the outcropping position of potential density surfaces and the associated change in surface buoyancy forcing. The water mass analysis is a diagnostic tool showing consistency between the two analysis methods. It is fundamentally problematic to separate wind and buoyancy forcing in a coupled climate model to distinguish relative contributions to changes in the MOC and ACC transport. Ultimately, in this model, the wind is responsible for the changes in the MOC and ACC transport since this is the perturbed variable. Our results suggest a key role for the ocean since changes to SST distributions (Fig. 11c) are accompanied by changes to surface heating and cooling (Fig. 12c) that dominate the surface buoyancy flux (Fig. 12a).

In this study we have simulated a ~21-yr perturbation to the Southern Ocean that resolves mesoscale eddies. This simulation pushed the limits of the community's current computational capabilities. Ideally, analyzing the full response of the overturning circulation to a perturbation of this type would require a simulation that is at least an order of magnitude longer. Thus, parameterization of mesoscale processes is still needed. This simulation, however, does support the study of Thompson and Garabato (2014), which suggests that the

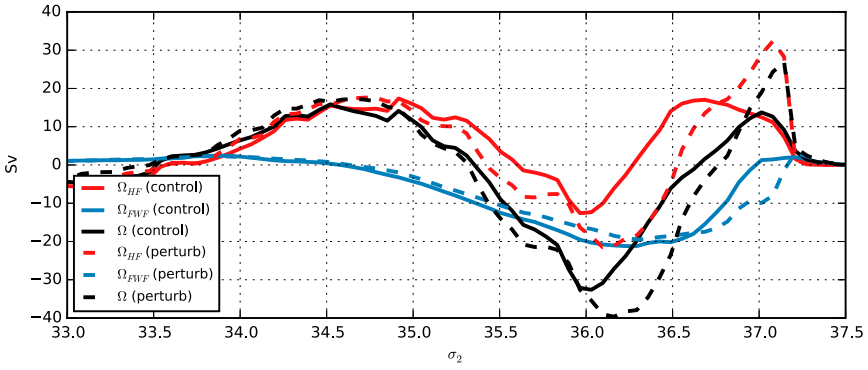

FIG. 14. Surface water mass transformation in control (solid) and perturbation (dashed) experiments. The heat-flux-driven transformation is in red, the freshwater-flux-driven transformation is in blue, and the net transformation is in black. Positive values mean indicate water being made denser.

equilibration of the ACC to changes in surface wind forcing will principally involve processes that are zonally asymmetric. A change in the wind stress without an increase in the zonal-mean transport requires a greater vertical momentum flux carried out by transient eddies. Thompson and Garabato (2014) argue that changes in eddy activity will be focused in standing meanders related to fluctuations in the amplitude and wavelength of the meander. It is important to note that this response is quite different from the coarse-resolution study of GD11, where the GM coefficient increases almost uniformly throughout the ACC. A key result of this study is that directly resolving mesoscale eddies shows that the response of ACC's EKE, for instance, to changes in wind stress, is likely too nuanced to be described by trends spanning the whole ACC or even basins. We plan to analyze the momentum and vorticity budgets of both high- and low-resolution simulations, similar to Cronin and Watts (1996) and Hughes (2005) in a future study.

There are some potential shortcomings of our simulation. One shortcoming is the shortness of the WP experiment. It is possible that there is decadal variability, but this is not possible to assess in a ~21-yr record. Another shortcoming is that the analysis was done using monthly archived data. Ballarotta et al. (2013) found close correspondence in the MOC at 5-day versus monthly archived data, suggesting that most of the signal is at monthly time scales and longer. However, their analysis was done in an eddy-permitting model (0.25°), which does not adequately resolve the first baroclinic deformation radius at these latitudes (Hallberg 2013). Encouragingly, Abernathey and Wortham (2015), analyzing the same class of CESM simulation used here, found that mesoscale eddy fluxes were dominated by submonthly frequencies. Future studies, for example, could focus on longer simulations, meridional shifts of the mean winds to simulate past climates, and increases in vertical resolution.

With these caveats set aside, the high-resolution simulation has shown how increasing winds could lead to an increase in the MOC over the time scales of 20 yr. The results from this study broadly agree with ozone depletion experiments, meant to simulate the increase in zonal wind stress in the Southern Hemisphere during austral summer (Ferreira et al. 2015; Solomon et al. 2015). The average SST difference during the last 10 yr of our WP experiment resemble the slow time-scale response in Ferreira et al. (2015), in which there is warming around Antarctica and cooling at midlatitudes (Fig. 11c). The wind stress changes are stronger in our WP experiment than in the ozone depletion studies, and as a result we see much more warming, up to 2°C, in places around Antarctica. These results are indicative of an increase in the lower cell of the MOC (Fig. 8), which causes more upwelling of warm and salty Circumpolar Deep Water (CDW). The upwelling of CDW melts more sea ice throughout the year, which leads to an enhancement of FWFs surrounding Antarctica. The recent trends in winds observed over the past few decades in Southern Hemisphere winds may already be having an influence on the MOC. This would infer that the oceanic uptake of CO_2 may be changing as well.

Acknowledgments. S.P.B. was supported by the President and Director's Fund at the California Institute of Technology. A.F.T. was supported by NSF Grant NSF OCE-1235488. This manuscript was greatly improved by comments from Andy Hogg and an anonymous reviewer. We thank Justin Small for providing the control experiment. Computational resources for the simulation analyzed here were provided by the NCAR Computational and Information Systems Lab under the

"Accelerated Scientific Discovery" program. We also thank Marcus Jochum for helpful comments that improved the manuscript and technical support from Gokhan Danabasoglu.

REFERENCES

Abernathey, R., and P. Cessi, 2014: Topographic enhancement of eddy efficiency in baroclinic equilibration. *J. Phys. Oceanogr.*, **44**, 2107–2126, doi:10.1175/JPO-D-14-0014.1.

——, and C. Wortham, 2015: Phase speed cross spectra of eddy heat fluxes in the pacific. *J. Phys. Oceanogr.*, **45**, 1285–1301, doi:10.1175/JPO-D-14-0160.1.

——, J. Marshall, and D. Ferreira, 2011: The dependence of Southern Ocean meridional overturning on wind stress. *J. Phys. Oceanogr.*, **41**, 2261–2278, doi:10.1175/JPO-D-11-023.1.

Abram, N. J., R. Mulvaney, F. Vimeux, S. J. Phipps, J. Turner, and M. H. England, 2014: Evolution of the Southern Annular Mode during the past millennium. *Nat. Climate Change*, **4**, 564–569, doi:10.1038/nclimate2235.

Ballarotta, M., S. Drijfhout, T. Kuhlbrodt, and K. Döös, 2013: The residual circulation of the Southern Ocean: Which spatio-temporal scales are needed? *Ocean Modell.*, **64**, 46–55, doi:10.1016/j.ocemod.2013.01.005.

Bishop, S. P., and F. O. Bryan, 2013: A comparison of mesoscale eddy heat fluxes from observations and a high-resolution ocean model simulation of the Kuroshio Extension. *J. Phys. Oceanogr.*, **43**, 2563–2570, doi:10.1175/JPO-D-13-0150.1.

Böning, C. W., A. Dispert, M. Visbeck, S. R. Rintoul, and F. U. Schwarzkopf, 2008: The response of the Antarctic Circumpolar Current to recent climate change. *Nat. Geosci.*, **1**, 864–869, doi:10.1038/ngeo362.

Bryan, F. O., P. R. Gent, and R. Tomas, 2014: Can Southern Ocean eddy effects be parameterized in climate models. *J. Climate*, **27**, 411–425, doi:10.1175/JCLI-D-12-00759.1.

Chidichimo, M. P., K. A. Donohue, D. R. Watts, and K. L. Tracey, 2014: Baroclinic transport time series of the Antarctic Circumpolar Current measured in Drake Passage. *J. Phys. Oceanogr.*, **44**, 1829–1853, doi:10.1175/JPO-D-13-071.1.

Cronin, M., and D. R. Watts, 1996: Eddy-mean flow interaction in the Gulf Stream at 68°W. Part I: Eddy energetics. *J. Phys. Oceanogr.*, **26**, 2107–2131, doi:10.1175/1520-0485(1996)026<2107:EFIITG>2.0.CO;2.

de Szoeke, R. A., and M. D. Levine, 1981: The advective flux of heat by mean geostrophic motions in the Southern Ocean. *Deep-Sea Res.*, **28A**, 1057–1085, doi:10.1016/0198-0149(81)90048-0.

Döös, K., and D. J. Webb, 1994: The Deacon cell and the other meridional cells of the Southern Ocean. *J. Phys. Oceanogr.*, **24**, 429–442, doi:10.1175/1520-0485(1994)024<0429:TDCATO>2.0.CO;2.

Downes, S. M., and A. M. Hogg, 2013: Southern Ocean circulation and eddy compensation in CMIP5 models. *J. Climate*, **26**, 7198–7220, doi:10.1175/JCLI-D-12-00504.1.

——, A. Gnanadesikan, S. Griffies, and J. Sarmiento, 2011: Water mass exchange in the Southern Ocean in coupled climate models. *J. Phys. Oceanogr.*, **41**, 1756–1771, doi:10.1175/2011JPO4586.1.

Dufour, C., J. L. Sommer, J. Zika, M. Gehlen, J. Orr, P. Mathiot, and B. Barnier, 2012: Standing and transient eddies in the response of the Southern Ocean meridional overturning to the Southern Annular Mode. *J. Climate*, **25**, 6958–6974, doi:10.1175/JCLI-D-11-00309.1.

Farneti, R., and Coauthors, 2015: An assessment of Antarctic Circumpolar Current and Southern Ocean meridional overturning circulation sensitivity during 1958–2007 in a suite of interannual CORE-II simulations. *Ocean Modell.*, **93**, 84–120, doi:10.1016/j.ocemod.2015.07.009.

Ferreira, D., J. Marshall, C. M. Bitz, S. Solomon, and A. Plumb, 2015: Antarctic ocean and sea ice response to ozone depletion: A two-time-scale problem. *J. Climate*, **28**, 1206–1226, doi:10.1175/JCLI-D-14-00313.1.

Firing, Y. L., T. K. Chereskin, and M. R. Mazloff, 2011: Vertical structure and transport of the Antarctic Circumpolar Current in Drake Passage from direct velocity observations. *J. Geophys. Res.*, **116**, C08015, doi:10.1029/2011JC006999.

Gent, P. R., 2016: Effects of Southern Hemisphere wind changes on the meridional overturning circulation in ocean models. *Annu. Rev. Mar. Sci.*, **8**, 79–94, doi:10.1146/annurev-marine-122414-033929.

——, and J. C. McWilliams, 1990: Isopycnal mixing in ocean circulating models. *J. Phys. Oceanogr.*, **20**, 150–155, doi:10.1175/1520-0485(1990)020<0150:IMIOCM>2.0.CO;2.

——, and G. Danabasoglu, 2011: Response to increasing Southern Hemisphere winds in CCSM4. *J. Climate*, **24**, 4992–4998, doi:10.1175/JCLI-D-10-05011.1.

——, and Coauthors, 2011: The Community Climate System Model version 4. *J. Climate*, **24**, 4973–4991, doi:10.1175/2011JCLI4083.1.

Gnanadesikan, A., M.-A. Pradal, and R. Abernathey, 2015: Isopycnal mixing by mesoscale eddies significantly impacts oceanic anthropogenic carbon uptake. *Geophys. Res. Lett.*, **42**, 4249–4255, doi:10.1002/2015GL064100.

Hallberg, R., 2013: Using a resolution function to regulate parameterizations of oceanic mesoscale eddies. *Ocean Modell.*, **72**, 92–103, doi:10.1016/j.ocemod.2013.08.007.

——, and A. Gnanadesikan, 2006: The role of eddies in determining the structure and response of wind-driven Southern Hemisphere overturning: Results from the modeling eddies in the Southern Ocean (MESO) project. *J. Phys. Oceanogr.*, **36**, 2232–2252, doi:10.1175/JPO2980.1.

Hogg, A. M., M. P. Meredith, D. P. Chambers, E. P. Abrahamsena, C. W. Hughes, and A. K. Morrison, 2015: Recent trends in the Southern Ocean eddy field. *J. Geophys. Res.*, **120**, 257–267, doi:10.1002/2014JC010470.

Hughes, C., 2005: Nonlinear vorticity balance of the Antarctic Circumpolar Current. *J. Geophys. Res.*, **110**, C11008, doi:10.1029/2004JC002753.

Hunke, E., and W. Lipscomb, 2008: CICE: The Los Alamos sea ice model: Documentation and software user's manual, version 4.0. Los Alamos National Laboratory Tech. Rep. LA-CC-06-012, 116 pp.

Hurrell, J. W., and Coauthors, 2013: The Community Earth System Model: A framework for collaborative research. *Bull. Amer. Meteor. Soc.*, **94**, 1339–1360, doi:10.1175/BAMS-D-12-00121.1.

Iudicone, D., G. Madec, and T. J. McDougall, 2008: Water-mass transformations in a neutral density framework and the key role of light penetration. *J. Phys. Oceanogr.*, **38**, 1357–1376, doi:10.1175/2007JPO3464.1.

Johnson, G. C., and H. L. Bryden, 1989: On the size of the Antarctic Circumpolar Current. *Deep-Sea Res.*, **36**, 39–53, doi:10.1016/0198-0149(89)90017-4.

Kirtman, B., and Coauthors, 2012: Impact of ocean model resolution on CCSM climate simulations. *Climate Dyn.*, **39**, 1303–1328, doi:10.1007/s00382-012-1500-3.

Langlais, C. E., S. R. Rintoul, and J. D. Zika, 2015: Sensitivity of Antarctic Circumpolar Current transport and eddy activity to wind patterns in the Southern Ocean. *J. Phys. Oceanogr.*, **45**, 1051–1067, doi:10.1175/JPO-D-14-0053.1.

Large, W. G., and A. J. G. Nurser, 2001: Ocean surface water mass transformation. *Ocean Circulation and Climate: Observing and Modelling the Global Ocean*, Academic Press, 317–336.

——, and S. G. Yeager, 2009: The global climatology of an interannually varying air-sea flux data set. *Climate Dyn.*, **33**, 341–364, doi:10.1007/s00382-008-0441-3.

Lawrence, D., and Coauthors., 2011: Parameterization improvements and functional and structural advances in version 4 of the Community Land Model. *J. Adv. Model. Earth Syst.*, **3**, M03001, doi:10.1029/2011MS000045.

Lee, M., and A. Coward, 2003: Eddy mass transport for the Southern Ocean in an eddy-permitting global ocean model. *Ocean Modell.*, **5**, 249–266, doi:10.1016/S1463-5003(02)00044-6.

Lenn, Y.-D., T. K. Chereskin, J. Sprintall, and J. L. McClean, 2011: Near-surface eddy heat and momentum fluxes in the Antarctic Circumpolar Current in Drake Passage. *J. Phys. Oceanogr.*, **41**, 1385–1407, doi:10.1175/JPO-D-10-05017.1.

Marsh, R., A. J. G. Nurser, A. P. Megann, and A. L. New, 2000: Water mass transformation in the Southern Ocean of a global isopycnal coordinate GCM. *J. Phys. Oceanogr.*, **30**, 1013–1045, doi:10.1175/1520-0485(2000)030<1013:WMTITS>2.0.CO;2.

Marshall, J., and T. Radko, 2003: Residual-mean solutions for the Antarctic Circumpolar Current and its associated overturning circulation. *J. Phys. Oceanogr.*, **33**, 2341–2354, doi:10.1175/1520-0485(2003)033<2341:RSFTAC>2.0.CO;2.

——, and K. Speer, 2012: Closure of the meridional overturning circulation through Southern Ocean upwelling. *Nat. Geosci.*, **5**, 171–180, doi:10.1038/ngeo1391.

——, D. Olbers, H. Ross, and D. Wolf-Gladrow, 1993: Potential vorticity constraints on the dynamics and hydrography of the Southern Ocean. *J. Phys. Oceanogr.*, **23**, 465–487, doi:10.1175/1520-0485(1993)023<0465:PVCOTD>2.0.CO;2.

——, D. Jamous, and J. Nilsson, 1999: Reconciling thermodynamic and dynamic methods of computation of water-mass transformation rates. *Deep-Sea Res. I*, **46**, 545–572, doi:10.1016/S0967-0637(98)00082-X.

McClean, J., and Coauthors, 2011: A prototype two-decade fully-coupled fine-resolution CCSM simulation. *Ocean Modell.*, **39**, 10–30, doi:10.1016/j.ocemod.2011.02.011.

Meredith, M. P., and A. M. Hogg, 2006: Circumpolar response of Southern Ocean eddy activity to a change in the Southern Annular Mode. *Geophys. Res. Lett.*, **33**, L16608, doi:10.1029/2006GL026499.

Morrison, A. K., and A. M. Hogg, 2013: On the relationship between Southern Ocean overturning and ACC transport. *J. Phys. Oceanogr.*, **43**, 140–148, doi:10.1175/JPO-D-12-057.1.

——, T. L. Frölicher, and J. L. Sarmiento, 2015: Upwelling in the Southern Ocean. *Phys. Today*, **68**, 27–32, doi:10.1063/PT.3.2654.

Munday, D. R., H. L. Johnson, and D. P. Marshall, 2013: Eddy saturation of equilibrated circumpolar currents. *J. Phys. Oceanogr.*, **43**, 507–532, doi:10.1175/JPO-D-12-095.1.

Newsom, E., C. Bitz, F. Bryan, R. P. Abernathey, and P. Gent, 2016: Southern Ocean deep circulation and heat uptake in a high-resolution climate model. *J. Climate*, **29**, 2597–2619, doi:10.1175/JCLI-D-15-0513.1.

Nikurashin, M., and G. Vallis, 2012: A theory of the interhemispheric meridional overturning circulation and associated stratification. *J. Phys. Oceanogr.*, **42**, 1652–1667, doi:10.1175/JPO-D-11-0189.1.

Sallée, J.-B., R. J. Matear, S. R. Rintoul, and A. Lenton, 2012: Localized subduction of anthropogenic carbon dioxide in the Southern Hemisphere oceans. *Nat. Geosci.*, **5**, 579–584, doi:10.1038/ngeo1523.

Small, R. J., and Coauthors, 2014: A new high-resolution global climate simulation using Community Atmosphere Model version 5. *J. Adv. Model. Earth Syst.*, **6**, 1065–1094, doi:10.1002/2014MS000363.

Smith, K. S., 2007: The geography of linear baroclinic instability in Earth's oceans. *J. Mar. Res.*, **65**, 655–683, doi:10.1357/002224007783649484.

Solomon, A., L. Polvani, K. Smith, and R. Abernathey, 2015: The impact of ozone depleting substances on the circulation, temperature, and salinity of the Southern Ocean: An attribution study with CESM1 (WACCM). *Geophys. Res. Lett.*, **42**, 5547–5555, doi:10.1002/2015GL064744.

Speer, K., and E. Tziperman, 1992: Rates of water mass formation in the North Atlantic Ocean. *J. Phys. Oceanogr.*, **22**, 93–104, doi:10.1175/1520-0485(1992)022<0093:ROWMFI>2.0.CO;2.

Stewart, A. L., R. Ferrari, and A. F. Thompson, 2014: On the importance of surface forcing in conceptual models of the deep ocean. *J. Phys. Oceanogr.*, **44**, 891–899, doi:10.1175/JPO-D-13-0206.1.

Straub, D., 1993: On the transport and angular momentum balance of channel models of the Antarctic Circumpolar Current. *J. Phys. Oceanogr.*, **23**, 776–782, doi:10.1175/1520-0485(1993)023<0776:OTTAAM>2.0.CO;2.

Thompson, A. F., and A. C. N. Garabato, 2014: Equilibration of the Antarctic Circumpolar Current by standing meanders. *J. Phys. Oceanogr.*, **44**, 1811–1828, doi:10.1175/JPO-D-13-0163.1.

Thompson, D. W., S. Solomon, P. J. Kushner, M. H. England, K. M. Grise, and D. J. Karoly, 2011: Signatures of the Antarctic ozone hole in Southern Hemisphere surface climate change. *Nat. Geosci.*, **4**, 741–749, doi:10.1038/ngeo1296.

Toggweiler, J. R., 2009: Shifting Westerlies. *Science*, **323**, 1434–1435, doi:10.1126/science.1169823.

Treguier, A. M., and J. C. McWilliams, 1990: Topographic influences on wind-driven, stratified flow in a beta-plane channel: An idealized model for the Antarctic Circumpolar Current. *J. Phys. Oceanogr.*, **20**, 321–343, doi:10.1175/1520-0485(1990)020<0321:TIOWDS>2.0.CO;2.

——, J. L. Sommer, J. Molines, and B. D. Cuevas, 2010: Response of the Southern Ocean to the Southern Annular Mode: Interannual variability and multidecadal trend. *J. Phys. Oceanogr.*, **40**, 1659–1668, doi:10.1175/2010JPO4364.1.

Tziperman, E., 1986: On the role of interior mixing and air-sea fluxes in determining the stratification and circulation of the oceans. *J. Phys. Oceanogr.*, **16**, 680–693, doi:10.1175/1520-0485(1986)016<0680:OTROIM>2.0.CO;2.

Viebahn, J., and C. Eden, 2012: Standing eddies in the meridional overturning circulation. *J. Phys. Oceanogr.*, **42**, 1486–1508, doi:10.1175/JPO-D-11-087.1.

Volkov, D. L., L.-L. Fu, and T. Lee, 2010: Mechanisms of the meridional heat transport in the Southern Ocean. *Ocean Dyn.*, **60**, 791–801, doi:10.1007/s10236-010-0288-0.

Walin, G., 1982: On the relation between sea-surface heat flow and thermal circulation in the ocean. *Tellus*, **34A**, 187–195, doi:10.1111/j.2153-3490.1982.tb01806.x.

Ward, M. L., and A. M. Hogg, 2011: Establishment of momentum balance by form stress in a wind-driven channel. *Ocean Modell.*, **40**, 133–146, doi:10.1016/j.ocemod.2011.08.004.

Wolfe, C. L., and P. Cessi, 2010: What sets the strength of the middepth stratification and overturning circulation in eddying ocean models? *J. Phys. Oceanogr.*, **40**, 1520–1538, doi:10.1175/2010JPO4393.1.

Wolff, J.-O., E. Maier-Reimer, and D. J. Olbers, 1991: Wind-driven flow over topography in a zonal β-plane channel: A quasi-geostrophic model of the Antarctic Circumpolar Current. *J. Phys. Oceanogr.*, **21**, 236–264, doi:10.1175/1520-0485(1991)021<0236:WDFOTI>2.0.CO;2.

Zika, J. D., J. L. Sommer, C. O. Dufour, A. C. N. Garabato, and A. Blaker, 2013a: Acceleration of the Antarctic Circumpolar Current by wind stress along the coast of Antarctica. *J. Phys. Oceanogr.*, **43**, 2772–2784, doi:10.1175/JPO-D-13-091.1.

——, and Coauthors, 2013b: Vertical eddy fluxes in the Southern Ocean. *J. Phys. Oceanogr.*, **43**, 941–955, doi:10.1175/JPO-D-12-0178.1.